ARTICLE

Check for updates

Isotropic gap formation, localization, and waveguiding in mesoscale Yukawa-potential amorphous structures

Murat Can Sarihan [1,2✉], Alperen Govdeli[1], Zhihao Lan [3], Yildirim Batuhan Yilmaz[1], Mertcan Erdil[1], Yupei Wang[3], Mehmet Sirin Aras[2], Cenk Yanik [4], Nicolae Coriolan Panoiu [3✉], Chee Wei Wong [2✉] & Serdar Kocaman [1✉]

Amorphous photonic structures are mesoscopic optical structures described by electrical permittivity distributions with underlying spatial randomness. They offer a unique platform for studying a broad set of electromagnetic phenomena, including transverse Anderson localization, enhanced wave transport, and suppressed diffusion in random media. Despite this, at a more practical level, there is insufficient work on both understanding the nature of optical transport and the conditions conducive to vector-wave localization in these planar structures, as well as their potential applications to photonic nanodevices. In this study, we fill this gap by investigating experimentally and theoretically the characteristics of optical transport in a class of amorphous photonic structures and by demonstrating their use to some basic waveguiding nanostructures. We demonstrate that these 2-D structures have unique isotropic and asymmetric band gaps for in-plane propagation, controlled from first principles by varying the scattering strength and whose properties are elucidated by establishing an analogy between photon and carrier transport in amorphous semiconductors. We further observe Urbach band tails in these random structures and uncover their relation to frequency- and disorder-dependent Anderson-like localized modes through the modified Ioffe-Regel criterion and their mean free path - localization length character. Finally, we illustrate that our amorphous structures can serve as a versatile platform in which photonic devices such as disorder-localized waveguides can be readily implemented.

[1] Quantum Devices and Nanophotonics Research Laboratory, Department of Electrical and Electronics Engineering, Middle East Technical University, Ankara, Turkey. [2] Mesoscopic Optics and Quantum Electronics Laboratory, Department of Electrical and Computer Engineering, University of California Los Angeles, Los Angeles, CA, USA. [3] Department of Electronic and Electrical Engineering, University College London, Torrington Place, London WC1E 7JE, UK. [4] Sabanci University Nanotechnology Research and Application Center, Sabanci University, Istanbul, Turkey. ✉email: mcansarihan@ucla.edu; n.panoiu@ucl.ac.uk; cheewei.wong@ucla.edu; skocaman@metu.edu.tr

A longstanding view in photonics has been that disorder is an undesirable feature, primarily due to its detrimental effect of light scattering with increased optical losses. However, recently, an alternative view has been emerging, namely that the behavior of light in optical structures defined by random permittivity distributions could exhibit a variety of fascinating properties and thus offer new opportunities in photonics for fundamental and applied research[1–3]. For example, the existence of photonic band gaps in such disordered structures is somewhat counterintuitive, as the well-established paradigm had been that long-range periodic order was a prerequisite for the formation of band gaps via coherent wave scattering. Compared to the band gaps in photonic crystals (PhCs), which are highly anisotropic, band gaps in amorphous photonic structures are inherently isotropic and less sensitive to fabrication imperfections, thus providing improved functionality. Such isotropic band gaps of amorphous structures have been examined in the microwave[4,5] and visible wavelengths[6].

Amorphous photonic structures with artificially engineered disorder, characterized by random distributions of the refractive index, represent ideal platforms to study Anderson localization and related phenomena, such as enhanced or arrested wave transport[7–22]. The origins of wave transport and the presence of Anderson-like localization in 2D amorphous photonic structures are highly debated topics[17,23]. The role of short-range order in band gap formation is well-established[4,24], and the formation of band gaps under only short-range order is experimentally demonstrated in this article. Furthermore, a genuine Anderson localization transition was thought to occur only in 3D amorphous structures[25,26], while only infinite 2D structures can exhibit Anderson localization. This idea was challenged for out-of-plane (TM) polarization, where the scatterers behave as aligned in-plane monopoles, reducing the problem to scalar wave localization, for which Anderson transitions were observed in several studies[6,13,23,26]. For in-plane (TE) polarization, each scatterer acts like a dipole with a different orientation, which is essentially a vector-wave scattering phenomenon that long eluded the observation of localized states[17,27–29]. Finally, in a recent theoretical study, it was observed the presence of Anderson-like localization for TE (vector) waves in stealthy hyperuniform structures for a moderate density of scatterers. It was further demonstrated that hyperuniformity is not a prerequisite, the correlated disorder being sufficient to induce a transition to Anderson localization[23,27,30]. Here, we looked for the signatures of TE (vector) wave localization in Yukawa-potential amorphous structures.

Equally important, amorphous photonic structures have found technological applications in spectroscopy[31], random lasers[32,33], enhanced light-matter interactions[34–36], and topological photonics[37–41]. Furthermore, amorphous photonic structures could also provide new or improved functionalities to photonic integrated circuits, wherein their inherent randomness renders immaterial the influence of fabrication imperfections[42,43].

In this study, we examine first the formation and dependencies of band gaps in Yukawa potential amorphous structures, along with wave localization, modified Ioffe-Regel factors, and applications to photonic integrated circuits. In measurements and theory, we implement Yukawa potential amorphous structures (YPAS) with short-range order, known to have spatially homogeneous and isotropic frequency dispersion characteristics. We nanofabricated and characterized these amorphous photonic structures in slab and waveguide configurations in the near-infrared regime, and uncovered the band gaps and key wave transport character dependencies on frequency and disorder strength. Furthermore, we uncover similarities between the properties of band tails of electronic and photonic amorphous structures. We also examine the nature of in-plane-polarization (TE) mid-gap states, namely, we seek to clarify whether they are Anderson-like localized optical modes that satisfy the Ioffe-Regel criterion. The results presented here can provide general guidelines for designing photonic components based on amorphous structures, thus forming the basis for designing key building blocks such as beam splitters, mirrors, optical cavities, and random lasers with isotropic emission.

Results and discussion

Yukawa-potential amorphous photonic structures. The electrical permittivity distribution of the YPAS is generated using a Metropolis Monte Carlo algorithm sampling all configurations to construct a Markov chain for transition probabilities of each particle (hole)[6,44,45]. Consequently, the amorphous structure mimics the natural crystalline-to-glass transition of a semiconductor crystal, whereby each hole represents a point scattering particle in a colloidal, liquid-like structure, and the repulsive Yukawa potential governs the interaction between holes, $v(r) = (v_0/r) \exp(-r/r_s), r < r_0$[6,45]. Here, r_s is the screening length, and v_0 is a constant characterizing the strength of the potential. A critical parameter of the generation algorithm is the normalized temperature, $T^* = k_B T/v_0$, which quantifies the degree of randomness of a configuration. These parameters determine the Yukawa-potential equilibrium configuration, whose spatial characteristics are quantified by the average distance between the scatterers[46], normalized in this work to the lattice constant of a periodic hexagonal lattice. In Fig. 1a–c, an example of hole distributions for $T^* = 0.2$, $T^* = 0.8$, and $T^* = 5.0$ is given to emphasize the change in the equilibrium from low to high randomness.

To illustrate the unique features of YPASs, we compare in Fig. 1 the structural properties of periodic, disordered, and YPAS, quantified in both real and reciprocal spaces. The periodic structure is a hexagonal lattice with lattice constant, a, whereas the disordered structure is constructed from the periodic lattice by displacing each hole along the x- or y-axes by a quantity δ obeying a uniform random distribution defined in the interval, $[-0.25a/2, 0.25a/2]$ marked with a pseudo-temperature parameter 0.25 in Fig. 1e. The Yukawa-potential configurations are different from the periodic and disordered structures in several key aspects, which is apparent by performing a Fourier transform analysis of the resulting hole distributions[1,14,47–49]. The Fourier transform of periodic (Fig. 1d) and disordered (Fig. 1e) permittivity distributions have Bragg peaks, which is a signature of periodicity and long-range order. We note that, for the disordered structure, the added perturbation smears out and broadens the Bragg peaks, but their occurrence signifies that the underlying structure periodicity is preserved. The Fourier transform of the YPAS (Fig. 1f) noticeably, however, is isotropic and shows no local maxima.

The range of spatial order is characterized by the radial distribution function, $g(R)$, which is equal to the number dN of holes located in the annulus $(R, R + dR)$[50]. Specifically, as per Fig. 1(g), $g(R)$ shows discrete peaks even at large distances for the hexagonal lattice, confirming the long-range order. Upon adding disorder, these peaks begin to smear out, yet the underlying pattern is still preserved up to 10 unit distances, as per Fig. 1(h). In the amorphous structure, however, the peaks of the radial distribution function are attenuated and merged with the pedestal at about 5 unit distances (Fig. 1(i)), indicating the suppression of long-range order.

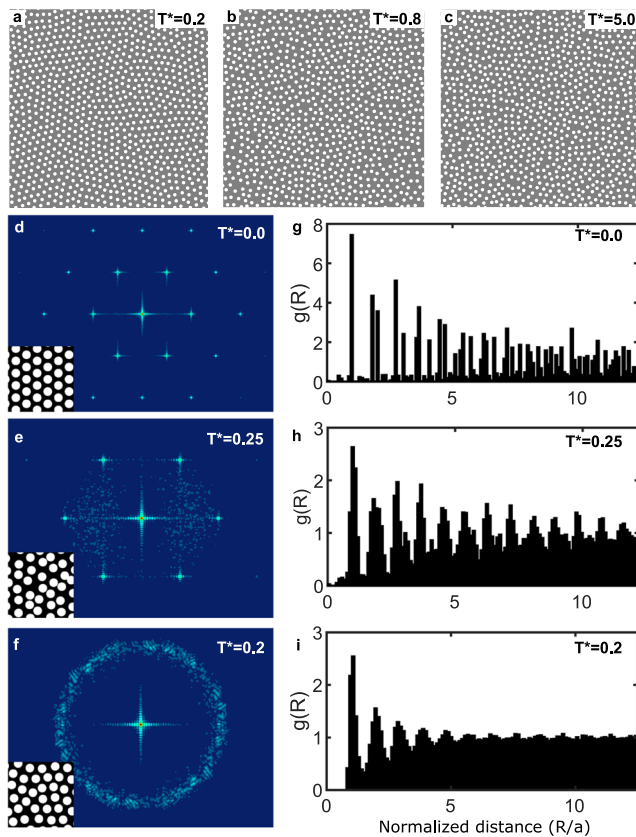**Isotropic band gap in the amorphous structures**. Previous studies at microwave frequencies showed that PhCs and

Fig. 1 Comparison of periodic and disordered lattices with Yukawa-potential amorphous structures. a–c The permittivity distributions, $\epsilon(x, y)$, correspond to amorphous structures with increasing randomness. The randomness is quantified by the normalized temperature T^*, which is given as (**a**) 0.2, (**b**) 0.8, and (**c**) 5.0. **d–f** Fourier transform of the periodic, disordered, and amorphous structures, respectively. $\epsilon(x, y)$ are shown in the insets with the silicon (etched air hole) regions depicted in black (white). The periodic photonic crystal has a hexagonal symmetry with lattice constant a, whereas the disordered structure is generated from the periodic lattice by randomly perturbing each hole (see text for details). For the amorphous structure, the hole distribution is generated using a Metropolis Monte Carlo sampling approach. The normalized temperature, T^*, in the three cases, has values of 0, 0.25, and 0.2, respectively. The value of (**e**) indicates the range of the added randomness to (**d**) in terms of ± 0.25*a introduced to show the difference between disordered and amorphous structures. **g–i** Corresponding radial distribution $g(R)$ of the air holes for the three lattice structures analyzed in **d–f**, respectively.

amorphous structures with the same characteristic length share the first band gap because in both cases, the band gap originates from short-range order[4,24]. Thus, we considered a reference PhC slab with a hexagonal lattice of air holes. Furthermore, for all three configurations (PhC, disordered, and amorphous structures), the characteristic length, a (i.e., the averaged nearest-neighbor distance between holes), slab thickness, h, and hole radius, r, are kept the same, so that in all three cases there is a common transverse-electric (TE) band gap. Here, TE mode designation is in accordance with photonic crystal slab terminology, where even modes are called TE-like and odd modes are called TM-like. According to our simulations, it is also possible to form TM (transverse-magnetic) band gap when dielectric rods are used inversely. For the parameters used in our experiments, namely $a = 400$ nm, $h = 220$ nm, and $r = 110$ nm, the mid-gap wavelength is about 1500 nm. Figure 2a shows the scanning

electron micrograph (SEM) of the amorphous structure with 400 nm average distance between holes, fabricated via electron-beam nanolithography followed by inductively coupled plasma reactive ion etching on silicon-on-insulator (SOI) wafers with 220 nm thickness of the silicon device layer. Each sample is suspended to form an air-bridge membrane with buffered oxide etch (BOE) and thus creates a symmetric planar membrane configuration.

The dispersive properties of our structures are investigated using finite-difference time-domain computations[51,52]. Figure 2b shows the computed transmission spectra of the PhC and amorphous structures. These spectra show that for the YPAS with $T^* = 0.4$ and $r = 110$ nm, the optical transmission is mainly independent of the propagation direction, the mobility edges fit for both x (blue) and y (red) directions, which matches with the overlapping photonic band gap of the PhC (green) illustrating that the structure is isotropic. In contrast, the PhC structure is highly anisotropic, with the transmission different along the $\Gamma - M$ and $\Gamma - K$ symmetry axes (detailed in Supplementary Note 1 and Fig. S2b). We note that, while the gap width is similar for both photonic structures, the isotropy provided by the YPAS can be employed to achieve all-angles broadband mirrors, devices with reduced angle sensitivity, and waveguiding along arbitrary directions.

For the $T^* = 0.2$ realization, the transmission is measured for two samples with hole radii of 110 nm and 120 nm, whereas for the $T^* = 0.4$ realization, transmission is measured for a sample with $r = 120$ nm in both x- and y- directions. All three measurements are depicted in Fig. 2c with solid blue lines. All the measured spectra match well with our simulation results (dashed red), where we extracted the actual hole positions and average hole radius from the SEM images of the device. The band tails are fitted between mid-gap and dielectric and air band edges according to the Urbach expression, $T \approx e^{(\lambda - \lambda_{midgap})/\Delta\lambda}$, where $\Delta\lambda$ is the effective width of the tail[53]. In this configuration, dielectric band tail widths are measured as 12.83 nm for $r = 110$ nm and 14.98 nm for $r = 120$ nm, for $T^* = 0.2$. For the air band tail, the change is more pronounced, 33.27 nm for $r = 110$ nm and 39 nm for $r = 120$ nm, indicating the higher density of localized states at the air band with larger holes. The tail widths are longer than the widths fitted in the numerical spectra, which might be due to fabrication-related disorders. In addition, we note that for the larger hole radius of 120 nm, a slight blue-shift of the mid-gap wavelength is observed, which agrees with predictions based on the perturbation theory for a larger radius, where a larger amount of dielectric material is removed from the homogeneous slab. When T^* increases from 0.2 to 0.4, the mid-gap wavelength remains largely unaffected (cf. Fig. 2(c)). Importantly, the spectra are asymmetric, displaying a steeper slope at the longer-wavelength edge. The origins of the longer-wavelength steeper slope and the mid-gap blue-shift are discussed together with the localization strength and air-dielectric band perturbation in the next subsection. For the $T^* = 0.2$ realization, the transmission is measured for two samples with hole radii of 110 nm and 120 nm, whereas for the $T^* = 0.4$ realization, transmission is measured for a sample with $r = 120$ nm in both x- and y- directions. All three measurements are depicted in Fig. 2c with solid blue lines. All the measured spectra match well with our simulation results (dashed red), where we extracted the actual hole positions and average hole radius from the SEM images of the device. The band tails are fitted between mid-gap and dielectric and air band edges according to the Urbach expression, $T \approx e^{(\lambda - \lambda_{midgap})/\Delta\lambda}$, where $\Delta\lambda$ is the effective width of the tail[53]. In this configuration, dielectric band tail widths are measured as 12.83 nm for $r = 110$ nm and 14.98 nm for $r = 120$ nm, for $T^* = 0.2$. For the air band tail, the
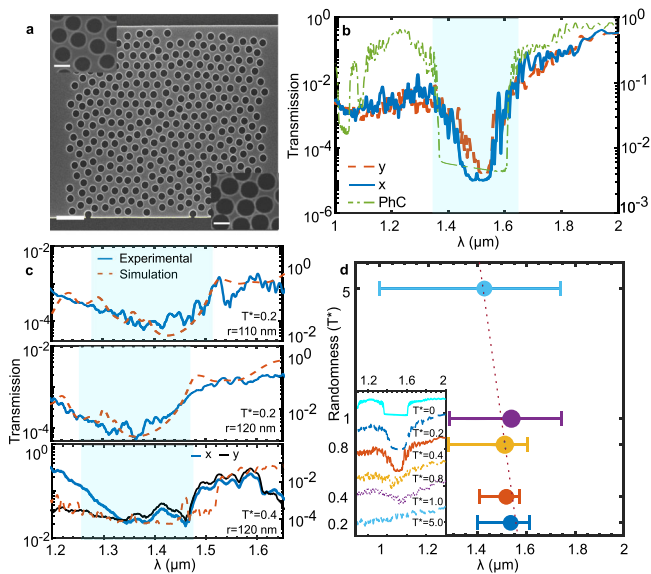
Fig. 2 Photonic band gaps in Yukawa-potential amorphous structures.
a Scanning electron micrograph (SEM) of an amorphous nanostructure
with $T^* = 0.2$, $r = 110$ nm, and $h = 220$ nm, fabricated onto a silicon-on-
insulator (SOI) wafer. Scale bar: 1 μm. Insets show zoom-in SEMs of two
structures with $r = 110$ nm (top left) and $r = 120$ nm (bottom right). Scale
bars: 250 nm. **b** Comparison of transmission spectra of the PhC and
amorphous structure with the same thickness and hole radius and with
$T^* = 0.4$. The latter are calculated for propagation along the x- and y-axes.
The right y-axis indicates the transmission in arbitrary units for the PhC
band gap (green) scaled to show the match between amorphous and PhC
band gaps. The cyan shade is a marker for the band gap region of the
reference photonic crystal. **c** Measured transmission spectra corresponding
to YPAS with $T^* = 0.2$ and hole radius of top: 110 nm and middle: 120 nm,
and with $T^* = 0.4$ and bottom: 120 nm respectively. The blue and black lines
are the experimentally measured spectra in x- and y- directions and
smoothed via Savitsky-Golay filtering; the red line is the numerically
computed spectra by importing the actual fabricated structure in the
software. The cyan shade is a marker for the band gap region. **d** Computed
band gap dependence on T^*, where the line bars indicate the region of
suppressed transmission according to 10-dB fall-off from the dielectric and
air band lev- els, while the circle pointer shows the minimum transmission
point. The dotted line is a guide to the eye. In the inset, the transmission
spectra determined for different values of T^* are shown by stacking each
line, whose y-axis values correspond to transmission in arbitrary values,
with the same scale for each line. The PhC slab corresponds to $T^* = 0$ and
for comparison purposes, the spectrum in this case and in **b** is determined
by averaging the PhC spectra over the propagation directions.

change is more pronounced, 33.27 nm for $r = 110$ nm and 39
nm for $r = 120$ nm, indicating the higher density of localized
states at the air band with larger holes. The tail widths are
longer than the widths fitted in the numerical spectra, which
might be due to fabrication-related disorders. In addition, we
note that for the larger hole radius of 120 nm, a slight blue-shift
of the mid-gap wavelength is observed, which agrees with
predictions based on the perturbation theory for a larger
radius, where a larger amount of dielectric material is removed
from the homogeneous slab. When T^* increases from 0.2 to 0.4,
the mid-gap wavelength remains largely unaffected (cf. Fig. 2c).
Importantly, the spectra are asymmetric, displaying a steeper
slope at the longer-wavelength edge. The origins of the longer-
wavelength steeper slope and the mid-gap blue-shift are
discussed together with the localization strength and air-
dielectric band perturbation in the next subsection.

In Fig. 2d, we examine the band gap widths for different values of
the normalized temperature, T^* (the degree of randomness increases
with T^*), with the corresponding transmission spectra plotted in the
inset. The mid-gap wavelengths are selected as the minimum
transmission point, while the gap boundaries are set according to 10-
dB fall-off from the dielectric and air band levels. We observe that the
band gap width for $T^* = 0.2$ and $T^* = 0.4$ has similar values and is
almost equal to that of the PhC ($T^* = 0$). At larger T^*, an increasing
number of localized states emerges inside the band gap and enhances
the light scattering. As a consequence, the transmission is suppressed
almost entirely. We further observe the localized-to-extended mode
transition with increasing T^*, where the increase in localized mode
density causes a reduction in the gap width of $T^* = 0.4$, from 215 nm
to 162 nm. However, at $T^* > 0.8$, we observe a shallow gap-like
regime where the transmission is suppressed only 10 dB compared to
dielectric and air bands. This localized-to-extended transition will be
examined further using effective modal width and localization
length. Moreover, we note that, with increasing T^*, the mid-gap
wavelength is slightly blue-shifted within a region of 1.45 and 1.5 μm,
due to the change in the lowest transmission point with localized-to-
extended mode transition. The only noticeable exception is $T^* = 1.0$,
where high statistical variations in the configuration change the
lowest transmission point. For our experimental measurements, we
chose $T^* = 0.2$ and $T^* = 0.4$, with hole radii of $0.275a$ and $0.3a$
respectively. The nanofabrication feasibility of the structures and
accessibility of probing the angular dependencies guided us in
choosing these values.

**Flexible waveguides with Yukawa-potential amorphous struc-
tures.** Following the experimental observation of photonic band
gaps and Anderson-like localization of YPAS, we demonstrate
next that such disordered optical media can be employed for
optical nanodevices, such as sub-wavelength waveguides. With
the isotropy of the band gap of the amorphous structures, the
orientation of the waveguide can be arbitrarily chosen. This is in
stark contrast with the case of 1D waveguides in PhC slabs, for
which the waveguide mode dispersion depends strongly on the
waveguide-wavevector orientation. Likewise, more complex
waveguide configurations, such as sharp bends and 1-to-N
splitters, can be readily implemented using our amorphous
materials. Note that to ensure that the waveguide has a constant
width, we added a row of equally spaced holes adjacently to both
sides of the waveguide[42], as per Fig. 3(b). Moreover, guided by
our previous simulations[43], the waveguide width, w, was opti-
mized so that the maximum transmission is achieved at the mid-
gap wavelength, a condition fulfilled for $w \approx 901$ nm (more
details on the waveguide design process are in our Supplemen-
tary Note 3). Figure 3a shows the simulated transmission spectra
of the optimized waveguide with different lengths, for
$r = 100$ nm. At the optimized mid-gap wavelength, the simula-
tion indicates a 0.5 dB insertion loss, without any noticeable
propagation loss up to 10.8 μm, a very promising result for chip-
scale applications.

Figure 3c shows the measured transmission spectrum for a
waveguide oriented along the x- and y-axis. We note that the
measured value of the 3 dB cutoff wavelength agrees well with the
simulation results presented in Fig. 2c. To further validate our
conclusions, we fabricated another waveguide in the same
amorphous structure with the same geometrical parameters,
except that it was oriented at an angle of 23 ° to the x-axis (see the
SEM in Fig. 3d). The corresponding transmission spectrum is
shown in Fig. 3e and is very similar to that presented in Fig. 3c in
terms of cutoff wavelength and baseband propagation loss. These
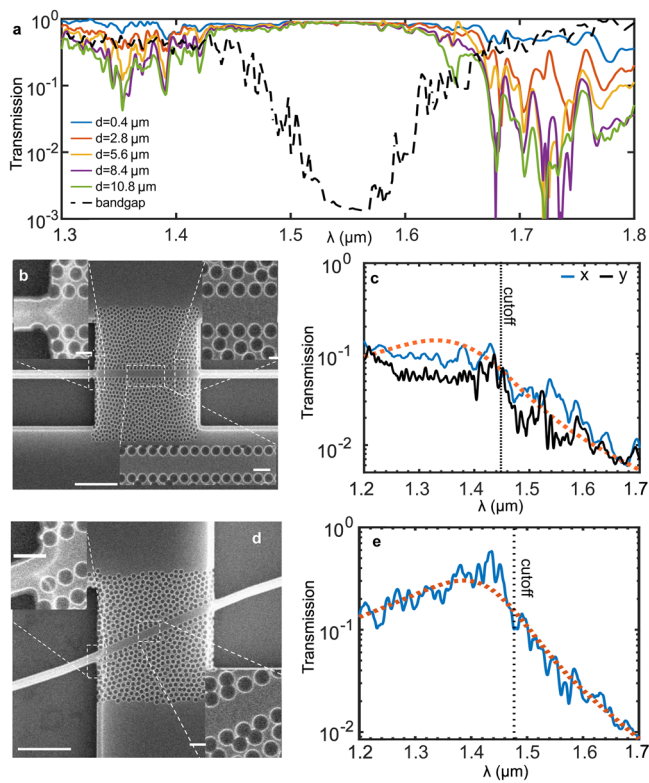results further support the band gap isotropy of our YPAS, which

Fig. 3 Experimental characterization of the band gap of Yukawa-potential amorphous structures and corresponding waveguides. a Transmission spectra of straight waveguides embedded in an amorphous structure with $w = 901$ nm and $r = 100$ nm. The dashed lines indicate the transmission spectra through a section of amorphous structure, whereas the distance from the excitation source is indicated in the legends. **b** Scanning electron microscopy (SEM) of an optical waveguide based on a YPAS with $T^* = 0.2$ and $r = 120$ nm. The waveguide is oriented along the x-axis and has a width of 901 nm. Scale bar: 5 μm. Insets show zoom-in SEMs of different regions of the waveguide. Scale bars: 500 nm. **c** Measured (blue and black lines) and fitted (red line) transmission spectra of the amorphous waveguide structure oriented along x-axis (blue) and y-axis (black). The 3 dB cutoff wavelength is ~1448 nm. **d** The same as in **b**, except that the waveguide is oriented at an angle of 23° with respect to the x-axis. **e** The same as in **c**, but for the waveguide in **d**. The 3 dB cutoff wavelength is ~1478 nm.

is the indispensable condition for long-sought complete band gaps in planar structures.

Anderson-like localization in Yukawa-potential amorphous structures. After investigating experimentally the formation of optically isotropic photonic band gaps in YPASs, we further analyzed the characteristics of optical transport in these structures theoretically. Of interest is the Anderson light localization in our YPASs. Particularly, the effective length of the local field distribution, L_{eff}, which quantifies the strength of the field localization and is defined as $L_{\text{eff}} \equiv P^{-1/2} = \{[\int I(\mathbf{r})^2 d\mathbf{r}]/[\int I(\mathbf{r}) d\mathbf{r}]^2\}^{-1/2}$. Here, $I(\mathbf{r})$ is the spatial distribution of the optical field, $\mathbf{r} = (x, y)$ is the in-plane position vector, and P is the inverse participation ratio[9]. The effective length was calculated for different values of the temperature T^*, and a statistical average over 10 samples was performed for each temperature. The effective length, whose wavelength dependence is depicted in Fig. 4a, varies linearly with the number of available states in the amorphous structure. The results in Fig. 4(a) show that inside the band gap L_{eff} increases with T^*, with an averaged mid-gap value of $L_{\text{eff}} = 1.93$ μm ≈ $5a$ being observed for

$T^* = 0.2$. Moreover, for the same T^*, L_{eff} decreases by about $3\times$ when the wavelength varies from the edge of the band gap to its center, underlying the transition of these edge modes away from weak localization and diffusive transport.

As can be seen in Fig. 4a, L_{eff} is smaller and more dispersive at the air-band edge (short-wavelength edge) of the band gap as compared to its behavior at the dielectric-band edge (long-wavelength edge). That is, there is spectral asymmetry with respect to the mid-gap, as noted earlier. A similar phenomenon is observed in condensed matter physics, where the transition of a liquefied crystalline semiconductor to a glassy medium is accompanied by the formation of what is known as Urbach tails[53,54]. They emerge when the valence and conduction bands begin to extend into the band gap due to the creation of localized trap states near the band edges. These exponential tails are revealed by the absorption spectra and are primarily determined by the thermal motion inside the lattice, disorder in the crystal structure, and impurity atoms[55]. From the tight-binding model, the valence (conduction) band is of bonding (antibonding) nature[54]. Moreover, the valence (conduction) tail states are associated with short (long) bonds inside the lattice, and since the short bonds are affected more by disorder, the corresponding states are more localized, and the valence band tail is broader[55]. In other words, the Urbach tails of the valence and conduction bands have different slopes; namely, the slope of the valence band tail is smaller than that of the conduction band tail[54]. This behavior is observed in our Yukawa-potential material, which can be viewed as a photonic analog of amorphous material in condensed matter physics.

As the plots presented in Figs. 2b and 4a suggest, the wavelength dependence of E-field localization within the air and dielectric band regions has different slopes. Specifically, for $T^* = 0.4$ case shown in Fig. 2b, the $1/e$ intensity fall-off length for the air band tail is 16.54 nm, whereas a steeper fall-off of 9.03 nm is observed for the dielectric band tail. Hence, the air band is more sensitive to perturbations, a result that can be explained as follows: for the air band, a more significant fraction of the E-field is located in the hole regions, and therefore, the perturbation associated with a random displacement of the location of the holes is more substantial in this case. As the wavelength increases across the band gap, the E-field is pushed into the dielectric regions. This behavior is similar to that seen in PhCs, where the difference between E-field localization corresponding to two consecutive bands leads to a band gap formation[56]. Moreover, as expected, the wavelength dependence of the E-field localization levels off as T^* increases. Note that the wavelength dependence of the H-field localization shows a behavior opposite to that of the E-field (detailed in Supplementary Note 1). In addition, this perturbation affects the modes in the air band more, leading to a more extensive spectral broadening of these modes. As a result, the air band tail would have a smaller slope as compared to that of the dielectric band, a conclusion fully supported by the transmission spectra in the subsequent Fig. 2b through 2d[9].

Now, let us examine the spatial distribution of the modes located inside the band gap and quantify their degree of localization. We first compute the optical modes of amorphous structures characterized by each T^*, and which are located in the region of the dielectric-band tail, i.e., close to the K-symmetry point. An example sampling of such modes is illustrated in Fig. 4b (detailed in Supplementary Note 2 and Figs. S5 and S6. From this set of modes, we select those with large Q-factor, which are presumably more localized (see the insets of Fig. 4c, d) and thus are not affected by the structure boundaries. Since we want to characterize structures ranging from weakly perturbed PhCs ($T^* \ll 1$) to YPAS with a large T^*, we used the modified Ioffe-
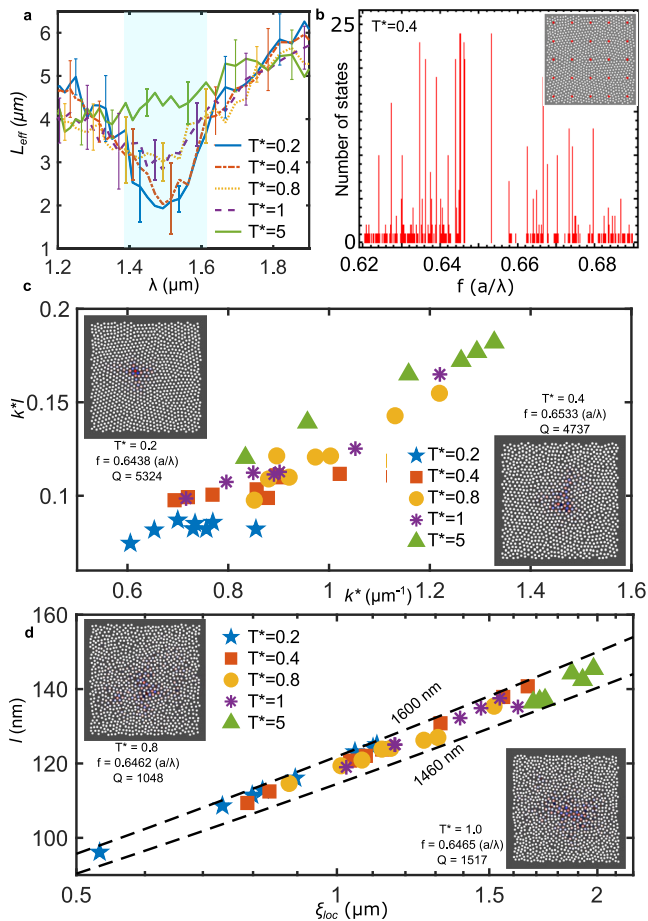
Fig. 4 Wave localization in Yukawa-potential amorphous structures.
a Wavelength dependence of the scattering length for different T^*. The error bars are the standard deviation of the effective length corresponding to a given T^* and to a set of multiple realizations of disorder. **b** Number of modes at the normalized frequencies above but the nearby edge of the dielectric band (K-point), for $T^* = 0.4$. The inset shows the modal probes used during calculations. **c** Modified Ioffe-Regel factor vs. the shifted wave number, k^*. **d** Mean free path vs. localization length, determined for the modes in **c**. The dashed lines correspond to the wavelengths of the top edge of the dielectric band ($\lambda = 1600$ nm) and mid-gap ($\lambda = 1460$ nm).The insets of (**c**) and (**d**) show example modal distributions of the modes with the highest quality factor (localization) from $T^* = 0.2$ to $T^* = 5.0$. A full list of the selected modes is given in Supplementary Note 2, Table S1.

Regel factor, k^*l[57], where $k^* = |k - k_{be}^K|$. Here, k is the wavenumber, k_{be}^K is the wavenumber of the dielectric-band edge (the K-point), and l is the mean free path. The modified Ioffe-Regel factor implicitly assumes the existence of a band gap, which strongly affects the free-photon density of states, while the scatterers are much smaller than the operating wavelength. Under these circumstances, the condition for the Anderson-like localization is $k^*l \simeq 1$.

The Ioffe-Regel factor of the selected modes, determined for different values of T^*, is presented in Fig. 4c. These plots reveal that the Ioffe-Regel factor is well below 1, indicating that the modes are truly localized Anderson modes. Moreover, the mode localization length, ξ_{loc}, can be determined by fitting the mode intensity profile to an exponential function, $I \sim \exp(-2r/\xi_{loc})$[9,58]. Consequently, the mean free path, l, can be obtained from the fitted parameter by the definition, $\xi_{loc} = l \exp(\pi kl/2)$, such that the modes in Fig. 4c can be represented in the $\xi_{loc} - l$ plane, as per Fig. 4d. From this figure,

one can see that ξ_{loc} increases with T^*, with l ranging from 100 nm to 150 nm. This is only a fraction of the lattice constant, a, whereas $\xi_{loc} \approx 1$ µm $= 2.5a$. This demonstrates that these states are indeed localized at the scale of the lattice constant. Note that these conclusions hold for the modes in the air-band tail, too.

Amorphous photonic structures have been largely overlooked when seeking to develop new photonic technologies, chiefly due to their complex fabrication and the statistical rather than deterministic nature of their properties. Contrary to this commonly adopted viewpoint, we demonstrate that amorphous photonic structures can be employed as a photonic material platform onto which planar photonic integrated circuits with complex configurations can be readily implemented. The key ingredient that makes this possible is the existence of an isotropic band gap originating from short-range order. Importantly, from a practical standpoint, the optical properties of these amorphous structures can be easily tuned by varying the two parameters that control their structure, namely the average inter-hole distance and effective temperature. This suggests that the amorphous photonic material platform introduced here can be used to implement key photonic devices, including Mach-Zehnder interferometers, multiplexers, and optical microcavities, and represents a practical testbed for new ideas emerging in the field of wave dynamics in random media.

Methods

Generation of amorphous photonic structure configurations. To investigate amorphous structures computationally, we employed a Monte Carlo algorithm for the generation of permittivity distributions that do not contain long-range order. For two-dimensional (2D) photonic crystal (PhC) slabs, one approximates rod or hole scatterers with hard disks or point particles located in the transverse $(x-y)$ plane, while along the z-axis, one imposes an index guiding condition. The flow of the Monte Carlo algorithm used to generate such amorphous photonic configurations is described below[44,46].

A. An input configuration is generated. In particular, we used as a starting structure a PhC slab configuration with a hexagonal lattice of air holes in a silicon slab. Using an ordered crystal lattice as a starting point allows one to use it as a reference periodic structure when investigating the transport properties of the resulting amorphous structure. Alternatively, a previously generated amorphous configuration can be used as a starting distribution, too, thus reaching equilibrium more rapidly. The potential energy of the initial configuration is calculated assuming that the inter-particle interactions in the system are described by a Yukawa-potential. Statistically, rules of canonical ensembles (constant number of elements N, volume V, and temperature T) are used.

B. A random displacement is applied to a scatterer, randomly selected from the distribution. The maximum allowed value of the displacement is adjusted so that it results in an acceptance displacement ratio, ρ, in the range of 40–60%. The difference in the potential energy of the configuration of scatterers, induced by this displacement, is then computed.

C. The acceptance ratio of displacements is determined using the probability calculated from the Metropolis criterion:

$$\rho_{i \to f} = \min\left(1, e^{-\frac{U_f - U_i}{k_B T}}\right), \quad (1)$$

where U_f and U_i are the system energies in the final (f) and initial (i) state, respectively.

D. The procedures described in steps B and C are repeated for different scatterers until equilibrium is reached. Specifically, the equilibrium is reached when the system energy converges to a

steady-state value, that is when the system energy no longer changes upon randomly displacing a scatterer.

Numerical methods. The photonic band structure of the reference PhC slab, for both the transverse magnetic (TM) and transverse electric (TE) polarizations, have been numerically calculated using MPB (MIT Photonic Bands) software[51]. Moreover, transmission spectra and local density of states (LDoS) were computed using the finite-difference-time-domain (FDTD) method implemented in MEEP (MIT Electromagnetic Equation Propagation) software[52]. Simulated transmission spectra are normalized using the output of a reference simulation of the same substrate without amorphous structure.

To study these mid-gap localized modes, we first probe them using the FDTD method implemented in MEEP[52]. Note that as these modes may be highly localized spatially, to effectively probe them, we set 25 probes covering the photonic structure uniformly, as illustrated in Fig. 4b. As field excitation, we used a source whose spectrum was broad enough to entirely cover the band gap. We used the Harminv procedure available in MEEP to analyze the spectral characteristics (normalized frequency, f, and quality factor, Q) of the localized modes. For effective localization length calculations, the integrals are performed in the transverse plane crossing through the middle of the amorphous crystal slab.

Supercontinuum transmission measurements. Using a NKT Photonics SuperKCompact supercontinuum light source, we have conducted a broadband spectral analysis of the fabricated structures. The laser was coupled to the amorphous structures and waveguides through an adiabatically tapered waveguide-lensed fiber system. The output is collected by a similar tapered waveguide-lensed fiber system. We analyzed the spectra collected by the fiber with a Thorlabs optical spectrum analyzer, whereas an InGaAs camera was used to monitor the optical coupling to the on-chip waveguides. For reference, the measured spectra were normalized to the output of channel waveguides with uniform cross-sections. Experimental data shown in Figs. 2 and 3 are given as normalized transmission ratio with the aforementioned method.

Data availability

The data that support the findings of this study are available from the authors upon reasonable request.

Code availability

The underlying code for this study is not publicly available but may be made available to qualified researchers upon reasonable request from the corresponding author.

References

1. Wiersma, D. S. Disordered photonics. *Nat. Photon.* **7**, 188 (2013).
2. Yu, S., Qiu, C.-W., Chong, Y., Torquato, S. & Park, N. Engineered disorder in photonics. *Nat. Rev. Mater.* **6**, 226 (2021).
3. Wiersma, D. S., Bartolini, P., Lagendijk, A. & Righini, R. Localization of light in a disordered medium. *Nature* **390**, 671 (1997).
4. Jin, C., Meng, X., Cheng, B., Li, Z. & Zhang, D. Photonic gap in amorphous photonic materials. *Phys. Rev. B* **63**, 195107 (2001).
5. Man, W. et al. Isotropic band gaps and freeform waveguides observed in hyperuniform disordered photonic solids. *Proc. Natl. Acad. Sci. USA* **110**, 15886 (2013).
6. Rechtsman, M. et al. Amorphous photonic lattices: band gaps, effective mass, and suppressed transport. *Phys. Rev. Lett.* **106**, 193904 (2011).
7. Sheinfux, H. H. et al. Observation of Anderson localization in disordered nanophotonic structures. *Science* **356**, 953–956 (2017).
8. De Raedt, H., Lagendijk, A. & De Vries, P. Transverse localization of light. *Phys. Rev. Lett.* **62**, 47 (1989).
9. Schwartz, T., Bartal, G., Fishman, S. & Segev, M. Transport and Anderson localization in disordered two-dimensional photonic lattices. *Nature* **446**, 52 (2007).
10. Riboli, F. et al. Anderson localization of near-visible light in two dimensions. *Opt. Lett.* **36**, 127 (2011).
11. Segev, M., Silberberg, Y. & Christodoulides, D. N. Anderson localization of light. *Nat. Photon.* **7**, 197 (2013).
12. Yang, J.-K. et al. Photonic-band gap effects in two-dimensional polycrystalline and amorphous structures. *Phys. Rev. A* **82**, 053838 (2010).
13. Conley, G. M., Burresi, M., Pratesi, F., Vynck, K. & Wiersma, D. S. Light transport and localization in two-dimensional correlated disorder. *Phys. Rev. Lett.* **112**, 143901 (2014).
14. Hsieh, P. et al. Photon transport enhanced by transverse Anderson localization in disordered superlattices. *Nat. Phys.* **11**, 268 (2015).
15. Boguslawski, M. et al. Analysis of transverse Anderson localization in refractive index structures with customized random potential. *Opt. Express* **21**, 31713 (2013).
16. Aubry, G. J. et al. Experimental tuning of transport regimes in hyperuniform disordered photonic materials. *Phys. Rev. Lett.* **125**, 127402 (2020).
17. Vynck, K. et al. Light in correlated disordered media. *Rev. Mod. Phys.* **95**, 045003 (2023).
18. Dikopoltsev, A., Sheinfux, H. H. & Segev, M. Localization by virtual transitions in correlated disorder. *Phys. Rev. B* **100**, 140202 (2019).
19. Barthelemy, P., Bertolotti, J. & Wiersma, D. S. A Lévy flight for light. *Nature* **453**, 495–498 (2008).
20. Levi, L. et al. Disorder-enhanced transport in photonic quasicrystals. *Science* **332**, 1541–1544 (2011).
21. Patsyk, A., Sivan, U., Segev, M. & Bandres, M. A. Observation of branched flow of light. *Nature* **583**, 60–65 (2020).
22. Levi, L., Krivolapov, Y., Fishman, S. & Segev, M. Hyper-transport of light and stochastic acceleration by evolving disorder. *Nat. Phys.* **8**, 912–917 (2012).
23. Monsarrat, R., Pierrat, R., Tourin, A. & Goetschy, A. Pseudogap and Anderson localization of light in correlated disordered media. *Phys. Rev. Res.* **4**, 033246 (2022).
24. Froufe-Pérez, L. S. et al. Role of short-range order and hyperuniformity in the formation of band gaps in disordered photonic materials. *Phys. Rev. Lett.* **117**, 053902 (2016).
25. Yamilov, A. et al. Anderson localization of electromagnetic waves in three dimensions. *Nat. Phys.* **19**, 1308–1313 (2023).
26. Haberko, J., Froufe-Pérez, L. S. & Scheffold, F. Transition from light diffusion to localization in three-dimensional amorphous dielectric networks near the band edge. *Nat. Commun.* **11**, 4867 (2020).
27. Scheffold, F., Haberko, J., Magkiriadou, S. & Froufe-Pérez, L. S. Light transport through amorphous photonic materials with localization and bandgap regimes. *Phys. Rev. Lett.* **129**, 157402 (2022).
28. Máximo, C. E., Piovella, N., Courteille, Ph. W., Kaiser, R. & Bachelard, R. Spatial and temporal localization of light in two dimensions. *Phys. Rev. A* **92**, 062702 (2015).
29. van Tiggelen, B. A. & Skipetrov, S. E. Longitudinal modes in diffusion and localization of light. *Phys. Rev. B* **103**, 174204 (2021).
30. Klatt, M. A., Steinhardt, P. J. & Torquato, S. Wave propagation and band tails of two-dimensional disordered systems in the thermodynamic limit. *Proc. Natl. Acad. Sci. USA* **119**, e2213633119 (2022).
31. Redding, B., Liew, S. F., Sarma, R. & Cao, H. Compact spectrometer based on a disordered photonic chip. *Nat. Photon.* **7**, 746 (2013).
32. Wiersma, D. S. The physics and applications of random lasers. *Nat. Phys.* **4**, 359 (2008).
33. Fazio, B. et al. Coherent backscattering of Raman light. *Nat. Photon.* **11**, 170–176 (2017).
34. Sapienza, L. et al. Cavity quantum electrodynamics with Anderson-localized modes. *Science* **327**, 1352 (2010).
35. Vynck, K., Burresi, M., Riboli, F. & Wiersma, D. S. Photon management in two-dimensional disordered media. *Nat. Mater.* **11**, 1017–1022 (2012).
36. Sharabi, Y., Sheinfux, H. H., Sagi, Y., Eisenstein, G. & Segev, M. Self-induced diffusion in disordered nonlinear photonic media. *Phys. Rev. Lett.* **121**, 233901 (2018).
37. Stützer, S. et al. Photonic topological Anderson insulators. *Nature* **560**, 461–465 (2018).
38. Zhou, P. et al. Photonic amorphous topological insulator. *Light: Sci. Appl.* **9**, 133 (2020).
39. Yang, B. et al. Topological states in amorphous magnetic photonic lattices. *Phys. Rev. B* **99**, 45307 (2019).
40. Bourne, C. & Prodan, E. Non-commutative Chern numbers for generic aperiodic discrete systems. *J. Phys. A: Math. Theor.* **51**, 235202 (2018).

41. Rechtsman, M. C. et al. Photonic Floquet topological insulators. *Nature* **496**, 196–200 (2013).
42. Miyazaki, H., Hase, M., Miyazaki, H. T., Kurokawa, Y. & Shinya, N. Photonic material for designing arbitrarily shaped waveguides in two dimensions. *Phys. Rev. B* **67**, 235109 (2003).
43. Sarihan, M. C. et al. *Optical Components and Materials XVI* (eds. M. J. Digonnet and S. Jiang) p. 35 (SPIE, 2019).
44. Frenkel, D. & Smit, B. *Understanding Molecular Simulation: From Algorithms To Applications* (Academic Press, 2001).
45. Hynninen, A.-P. & Dijkstra, M. Phase diagrams of hard-core repulsive Yukawa particles. *Phys. Rev. E* **68**, 21407 (2003).
46. Sarihan, M. C. *Photonic Integrated Circuit Components With Amorphous Structures*, Master's Thesis, (Middle East Technical University, 2018).
47. Gao, J. et al. Strongly coupled slow-light polaritons in one-dimensional disordered localized states. *Sci. Rep.* **3**, 1994 (2013).
48. Riboli, F. et al. Engineering of light confinement in strongly scattering disordered media. *Nat. Mater.* **13**, 720 (2014).
49. Rojas-Ochoa, L. F., Mendez-Alcaraz, J. M., Sáenz, J. J., Schurtenberger, P. & Scheffold, F. Photonic Properties of strongly correlated colloidal liquids. *Phys. Rev. Lett.* **93**, 073903 (2004).
50. Liu, M. Q., Zhao, C. Y., Wang, B. X. & Fang, X. Role of short-range order in manipulating light absorption in disordered media. *J. Opt. Soc. Am. B* **35**, 504 (2018).
51. Johnson, S. G. & Joannopoulos, J. D. Block-iterative frequency-domain methods for Maxwell's equations in a planewave basis. *Opt. Express* **8**, 173 (2001).
52. Oskooi, A. F. et al. Meep: a flexible free-software package for electromagnetic simulations by the FDTD method. *Comput. Phys. Commun.* **181**, 687 (2010).
53. Studenyak, I., Kranj, M. & Kurik, M. Urbach rule in solid state physics. *Int. J. Opt. Appl.* **4**, 76 (2014).
54. Fedders, P. A., Drabold, D. A. & Nakhmanson, S. Theoretical study on the nature of band-tail states in amorphous Si. *Phys. Rev. B* **58**, 15624 (1998).
55. Drabold, D. A., Li, Y., Cai, B. & Zhang, M. Urbach tails of amorphous silicon. *Phys. Rev. B* **83**, 045201 (2011).
56. Joannopoulos, J. D., Johnson, S., Winn, J. N., and Meade, R. D. *Photonic Crystals: Molding The Flow Of Light*. 2nd edn (Princeton University Press, 2008).
57. John, S. Localization of light. *Phys. Today* **44**, 32 (1991).
58. Lee, M. et al. Anderson localizations and photonic band-tail states observed in compositionally disordered platform. *Sci. Adv.* **4**, e1602796 (2018).

Acknowledgements

Author contributions

M.C.S., C.W.W., and S.K. designed and led the project. M.C.S. and Y.B.Y. designed the waveguide structures. M.C.S., Z.L., and Y.W. conducted numerical simulations and spectral analysis. M.S.A. and C.Y. performed the device nanofabrication. M.C.S., A.G., and M.E. conducted the measurements. M.C.S., N.C.P., C.W.W., and S.K. wrote the manuscript with contributions from all authors.

Competing interests

The authors declare no competing interests.

Additional information

Supplementary information The online version contains supplementary material available at https://doi.org/10.1038/s42005-023-01482-9.

Correspondence and requests for materials should be addressed to Murat Can Sarihan, Nicolae Coriolan Panoiu, Chee Wei Wong or Serdar Kocaman.

Peer review information *Communications Physics* thanks Arthur Goetschy, Pedro David García and the other, anonymous, reviewer(s) for their contribution to the peer review of this work. A peer review file is available.

Reprints and permission information is available at http://www.nature.com/reprints

Publisher's note Springer Nature remains neutral with regard to jurisdictional claims in published maps and institutional affiliations.

Supplementary information for: Isotropic gap formation, localization, and waveguiding in mesoscale Yukawa-potential amorphous structures

Murat Can Sarihan,[1, 2, *] Alperen Govdeli,[1] Zhihao Lan,[3] Yildirim Batuhan Yilmaz,[1] Mertcan Erdil,[1] Yupei Wang,[3] Mehmet Sirin Aras,[2] Cenk Yanik,[4] Nicolae Coriolan Panoiu,[3, †] Chee Wei Wong,[2, ‡] and Serdar Kocaman[1, §]

[1] *Quantum Devices and Nanophotonics Research Laboratory, Department of Electrical and Electronics Engineering, Middle East Technical University, Ankara, Turkey*

[2] *Mesoscopic Optics and Quantum Electronics Laboratory, Department of Electrical and Computer Engineering, University of California Los Angeles, Los Angeles, California, USA*

[3] *Department of Electronic and Electrical Engineering, University College London, Torrington Place, London WC1E 7JE, UK*

[4] *Sabanci University Nanotechnology Research and Application Center, Sabanci University, Istanbul, Turkey*

(Dated: 1 October 2023)

———

[*] Electronic mail: mcansarihan@ucla.edu

[†] Electronic mail: n.panoiu@ucl.ac.uk

[‡] Electronic mail: cheewei.wong@ucla.edu

[§] Electronic mail: skocaman@metu.edu.tr

Supplementary Note 1. NUMERICAL STUDIES ON PERIODIC AND AMORPHOUS STRUCTURES

Several examples of amorphous crystal configurations generated using the Monte Carlo algorithm, determined for different values of the normalized temperature, $T^* = k_B T$, are presented in Fig. S1. The design parameters of the properly designed photonic crystal (PhC) slabs were used to initialize the computational algorithm for the generation of the corresponding amorphous photonic structures. The photonic band diagram of a reference PhC slab with air holes arranged in a hexagonal lattice is shown in Fig. S2(a), where the band gap is indicated by the light-blue region. The transmission spectra of the PhC corresponding to the two principal symmetry axes, $\Gamma - M$ and $\Gamma - K$ are given in Fig. S2(b). As expected, they show pronounced anisotropy, both in terms of the spectral location of the edges of the corresponding band gap and the values of the transmission. In addition, in Fig. S2(c), we present the wavelength dependence of the local density of states (LDoS), determined for the PhC slab and an amorphous crystal with normalized temperature, $T^* = 0.4$.

The LDoS spectrum of the PhC (red line) shows clearly the location of the band edges with the associated singularities and a small number of states in the band gap. Note that the small but non-vanishingly number of states located in the band gap is due to finite-size effects in the simulated structure. The LDoS spectrum of a Yukawa-potential amorphous structure with $T^* = 0.4$ (blue line), which was vertically shifted to facilitate the comparison with the LDoS spectrum corresponding to the PhC case, has a band gap similar to that of the PhC (in terms of width and mid-wavelength). However, one can notice that two exponential
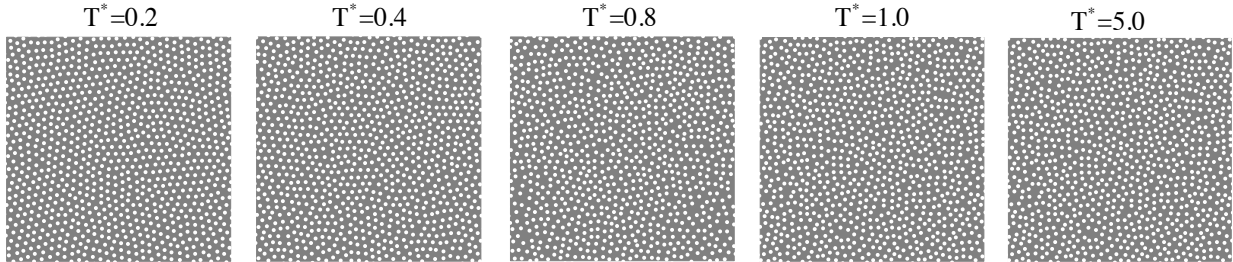

FIG. S1. Amorphous structure configurations generated using the Monte Carlo algorithm. The starting structure is a hexagonal PhC with $r = 0.1a$, whereas the normalized temperatures of the generated amorphous crystals are 0.2, 0.4, 0.8, 1.0 and 5.0.
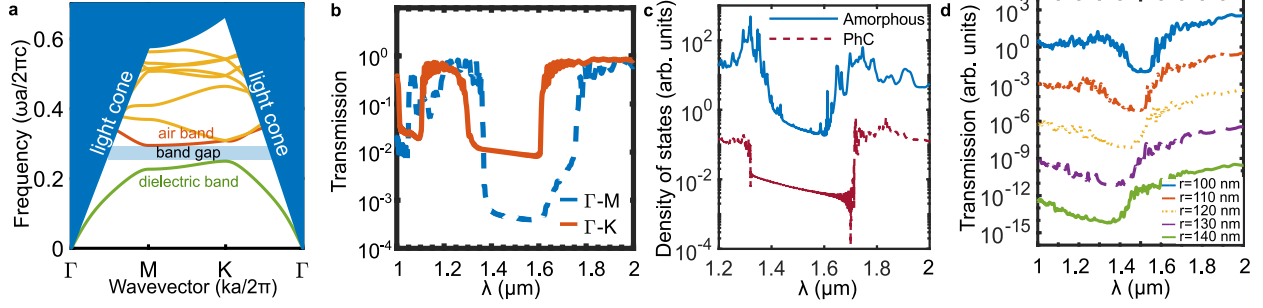
FIG. S2. (a) Band diagram of a PhC slab with thickness $h = 220\,\text{nm}$, consisting of a hexagonal lattice of air holes with lattice constant $a = 400\,\text{nm}$ and hole radius $r = 110\,\text{nm}$. (b) Numerical simulation of transmission spectra of the PhC slab given in (a), computed for the principal symmetry axes. (c) LDoS determined for an amorphous structure with $T^* = 0.4$ (blue line) and PhC (red line), both having $r = 100\,\text{nm}$. To facilitate their comparison, the spectra are offset vertically. The spectrum of the amorphous structure displays band tail states reminiscent of the Urbach tails observed in amorphous semiconductors. (d) Dependence of the transmission spectra on r, showing that the band-gap size and its mid-wavelength shifts with the hole radius from $1498\,\text{nm}$ to $1315\,\text{nm}$.

band tails are stretching from the band-gap edges all the way to the mid-gap region. As discussed in the main text, the two exponential band tails have different slopes, and certain analogies can be established between the physical mechanisms that lead to the formation of these band tails and those responsible for the emergence of valence and conduction band tails observed in amorphous semiconductors[7].

Figure S2(d) illustrates the variation of the band-gap of an amorphous crystal when the normalized hole radius, r/a, increases from 0.25 to 0.35 (hole radius varies from $100\,\text{nm}$ to $140\,\text{nm}$). When the hole radius increases, one observes that the band gap is blue-shifted, which is similar to what is observed in PhCs[5]. Furthermore, the slope of the air-band tail decreases when the hole radius increases. This is explained by the fact that, as the radius of the hole increases, the disorder increasingly affects the modes in the air-band tail, thus enhancing their spectral broadening. The opposite variation is observed in the case of the slope of the dielectric-band tail.

The Urbach band tails explained in the main text are studied by averaging the transmission spectra of multiple amorphous index distributions for $T^* = 0.2$ and $T^* = 0.4$ at
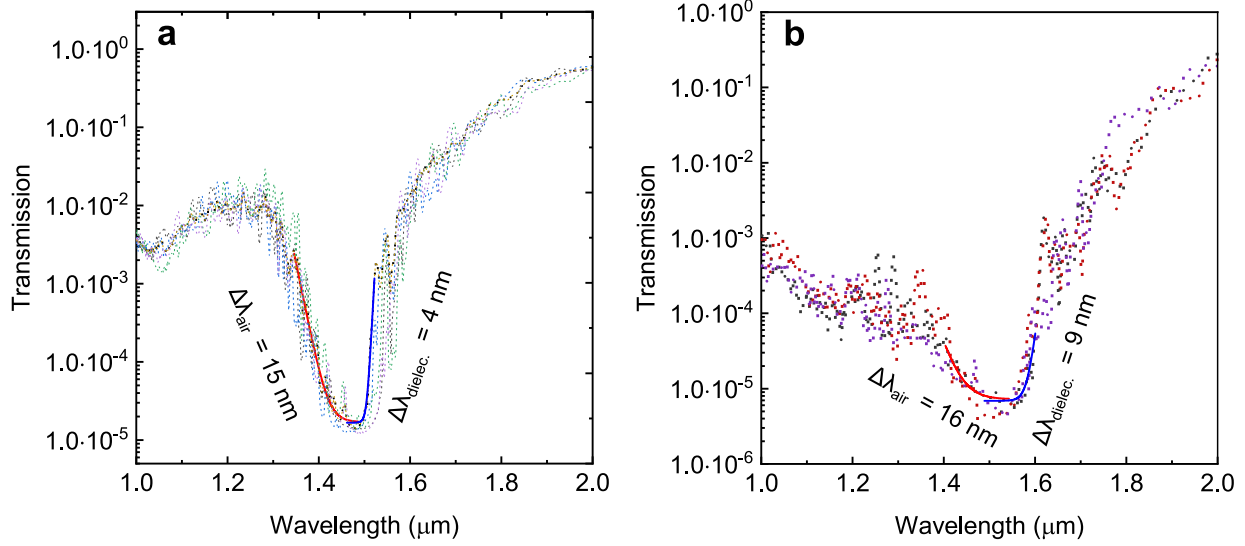
FIG. S3. Transmission spectrum for different realizations of amorphous structures with (a) $T^* = 0.2$ and (b) $T^* = 0.4$. Data points with different colors show different realizations, while the dielectric (blue) and air band (red) tails are fitted over the average spectrum. The band tails are fitted between the midgap and the band edge, and corresponding Urbach parameters are given in terms of wavelength.

Figure S3(a) and S3(b). The band tails are fitted between mid-gap and dielectric and air band edges according to the Urbach expression, $T \approx e^{(\lambda - \lambda_{midgap})/\Delta\lambda}$[7]. The band edges are determined according to the edge resonances similar to van Hove singularities observed in photonic crystals. The beginning of the band tail roughly corresponds to a 10-dB transmission suppression point compared to the air band, which is also used to determine the band-gap range in Figure 2(d). For $T^* = 0.2$, we obtained a dielectric band tail slope of 4 nm and an air band tail slope of 15 nm. When the disorder increases to $T^* = 0.4$, we observe the introduction of more localized states, pronounced by the increase in the dielectric and air band tails slopes to 9 nm and 16 nm. The introduction of localized states can be seen further in Figure S6.

The degree of localization inside the air regions of the electric (magnetic) field, η_e (η_h), is defined as the ratio between the energy of the electric (magnetic) field inside the air hole and the total energy on the electric (magnetic) field component of the corresponding mode[5]:
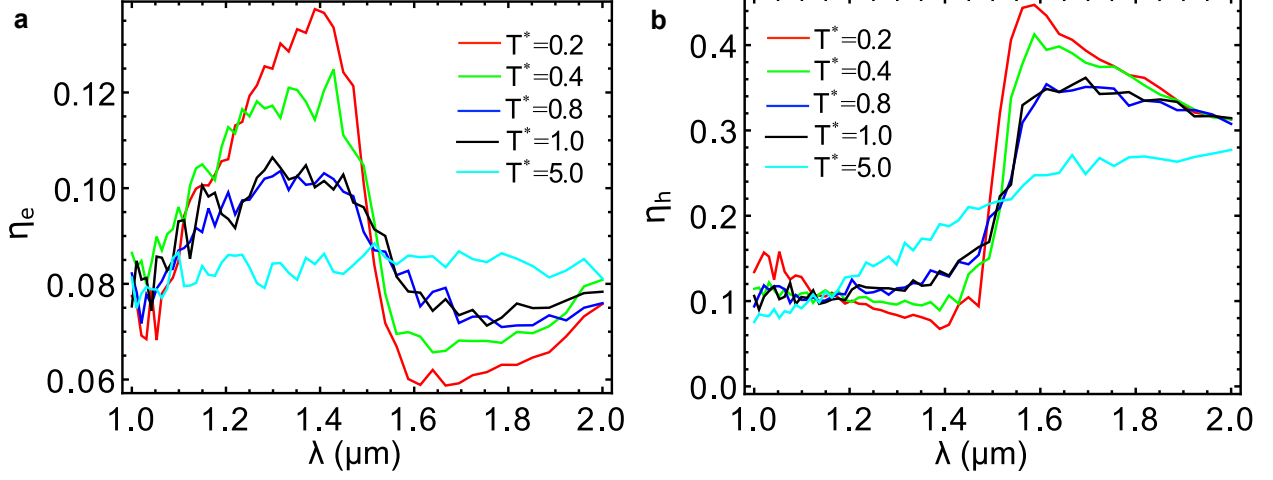
4

FIG. S4. Localization factor of the (a) electric and (b) magnetic field for different normalized temperature, T^*.

$$\eta_e = \frac{\int_{V_{\text{air}}} \epsilon_0 |\mathbf{E}(\mathbf{r})|^2 d\mathbf{r}}{\int_{V_{\text{tot}}} \epsilon(\mathbf{r}) |\mathbf{E}(\mathbf{r})|^2 d\mathbf{r}}, \tag{S1a}$$

$$\eta_h = \frac{\int_{V_{\text{air}}} \mu_0 |\mathbf{H}(\mathbf{r})|^2 d\mathbf{r}}{\int_{V_{\text{air}}} \mu(\mathbf{r}) |\mathbf{H}(\mathbf{r})|^2 d\mathbf{r}}, \tag{S1b}$$

where ϵ_0 and μ_0 are the vacuum electric permittivity and magnetic permeability, respectively.

The wavelength dependence of the localization factors η_e and η_h, determined for different values of T^*, are depicted in Fig. S4(a) and (b). As expected, they show opposite dependencies, i.e., whereas the E-field is more localized in the hole regions at shorter wavelengths, the opposite is true for the H-field. Moreover, when T^* increases, the wavelength dependence of the localization factors decreases significantly, especially in the case of the E-field. These results also indicate that a more pronounced band-gap is formed when the field localizations corresponding to the air and dielectric bands differ significantly[5].

The effective localization length, L_{eff}, of the optical field at a given frequency in a random photonic structure determines the mean scattering-free distance. A smaller effective length indicates a higher degree of localization[6]. This effective localization length is calculated using the following definition:

$$L_{\text{eff}} = \sqrt{\frac{[\int I(\mathbf{r}) d\mathbf{r}]^2}{\int I(\mathbf{r})^2 d\mathbf{r}}}, \tag{S2}$$

where $I(\mathbf{r}) = |\mathbf{E}(\mathbf{r})|^2$ is the intensity of the optical field and $\mathbf{r} = (x, y)$ is the in-plane position

vector. In our calculations, the integrals in Eq. (S2) were performed in the transverse plane crossing through the middle of the amorphous crystal slab.

The effective length provides valuable information about the degree of field localization inside the amorphous structure. A shorter effective length indicates a higher sensitivity to disorder for the air band and, consequently, a less steep air-band tail. Moreover, the effective length is longer at larger wavelengths, which correspond to the dielectric band, meaning that the optical field can propagate a longer distance in the structure, thus reducing the influence of disorder. More details regarding the relationship between the effective length and disorder strength, quantified by T^*, have been presented in the main text.

Supplementary Note 2.   CHARACTERIZATION OF ANDERSON LOCALIZED MODES

The Yukawa-potential amorphous structures investigated in this work possess Anderson localized modes with frequency inside the band gap. The optical modes near the edge of the dielectric band (i.e. near the K-symmetry point, whose normalized frequency is $f = 0.625$), determined for different values of the normalized temperature T^* using this procedure, are also given in Fig. S5. One can see that at low T^*, there are well-localized modes within the band-gap, and as T^* increases, more modes emerge more deeply inside the band-gap.

To study the localization properties of these mid-gap localized modes, we chose certain well-resolved modes at different T^* and calculated their frequency and Q-factor. The results of these calculations are summarized in Table S1. One can see that as T^* increases, the Q-factor of the modes tends to decrease and they become more extended (see the mode profiles in Fig. S6). These localized modes are further analyzed by independently exciting

TABLE S1. Selected band-gap modes near the edge of the dielectric band, i.e. located near the K-symmetry point, determined for different T^*, where f is the normalized frequency and Q is the quality factor.

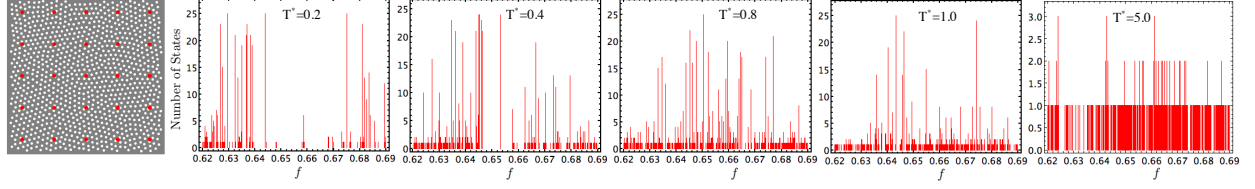| T^*	mode number: f (Q)							
	1	2	3	4	5	6	7	8
0.2	0.6297 (3629)	0.6324 (1092)	0.6350 (2773)	0.6367 (4429)	0.6370 (2750)	0.6382 (1479)	0.6390 (3642)	0.6438 (5324)
0.4	0.6347 (1264)	0.6362 (1671)	0.6390 (676)	0.6439 (2310)	0.6452 (1842)	0.6462 (2252)	0.6464 (2875)	0.6533 (4737)
0.8	0.6437 (842)	0.6453 (734)	0.6462 (1048)	0.6476 (954)	0.6505 (1036)	0.6523 (890)	0.6595 (908)	0.6645 (799)
1.0	0.6360 (608)	0.6405 (730)	0.6435 (1249)	0.6459 (1164)	0.6465 (1517)	0.6551 (991)	0.6646 (849)	0.6744 (1162)
5.0	0.6240 (204)	0.6427 (224)	0.6496 (278)	0.6611 (281)	0.6670 (296)	0.6688 (240)	0.6707 (172)	0.6816 (385)

FIG. S5. Top left corner panel depicts schematically the setup used to probe the mid-gap localized modes. The red dots indicate the location of the probes. The other panels show the number of modes located above but nearby the edge of the dielectric band (K-point), computed for different T^*. The normalized frequency is $f = 1\,\mu\text{m}/\lambda$, where λ is the wavelength in vacuum.
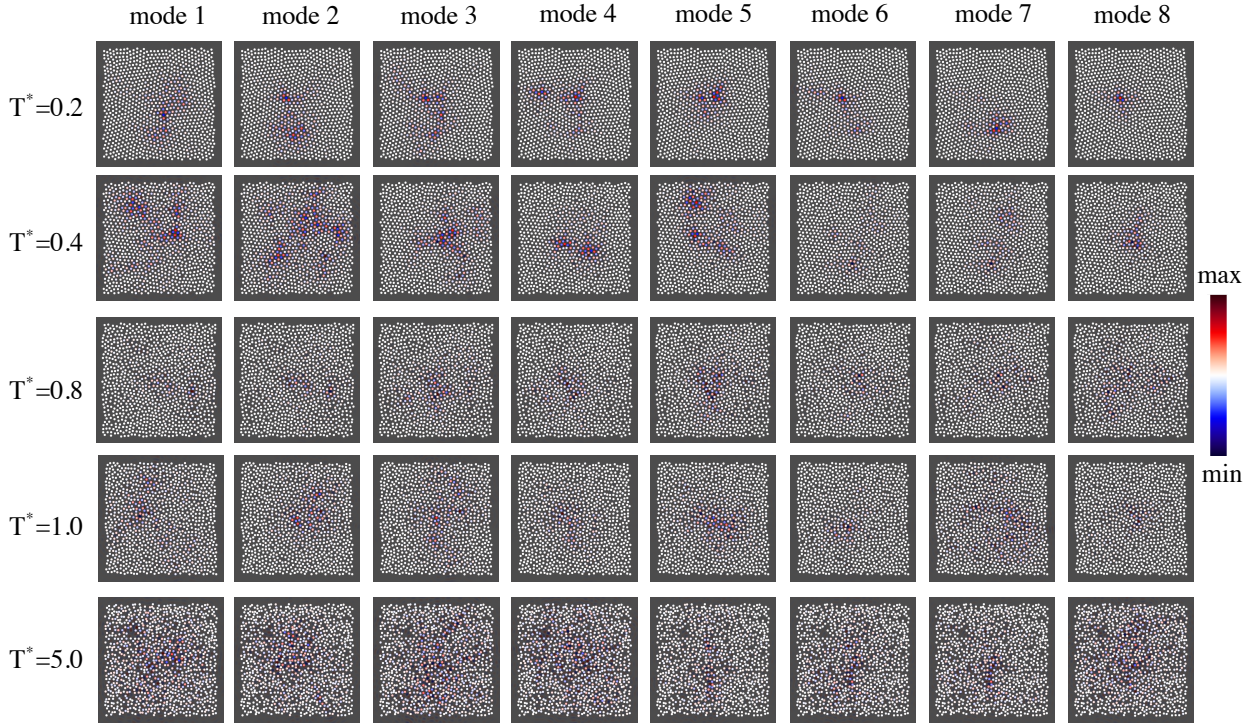

FIG. S6. Spatial distribution of H_z of the modes listed in Table S1, computed in the transverse plane crossing through the middle of the photonic slab.

them using a continuous-wave source whose frequency is equal to the frequency of the mode under investigation. The field profiles of these modes are shown in Fig. S6, from which one can see that at low T^*, the modes become more localized when moving away from the edge of the dielectric band (i.e., when their frequency f increases away from the frequency corresponding to the K-symmetry point of the dielectric band). For example, compare the field profiles of modes 8 and 1 at $T^* = 0.2$. As T^* increases, that is, when the strength of

disorder increases, the field profiles become more extended as the corresponding mean free path increases, too. A more detailed discussion of localization properties of the Anderson modes, based on physical quantities such as the Ioffe-Regel factor, localization length, and mean free path, have been presented in the main text.

Supplementary Note 3.   DESIGN OF WAVEGUIDES IN AMORPHOUS STRUCTURES

Waveguides in amorphous photonic structures were constructed by removing a set of holes, which defines the desired waveguide area and configuration. Due to the randomized positions of holes in the amorphous crystal, generally, one would end up with small variations of the waveguide width along the waveguide. To avoid the optical losses due to wave scattering induced by these random width variations, we added two rows of equally spaced holes adjacently to both sides of the waveguide[8], the distance between adjacent holes being equal to the lattice constant, a, used in the design of the reference PhC. This method was shown to greatly facilitate the design of arbitrarily-shaped waveguides embedded in uniform random distributions of scatterers[8].

It is well known that the width of a one-dimensional PhC optical waveguide plays a key role in determining its frequency dispersion properties, especially when the waveguide is operated in the subwavelength regime. Therefore, using numerical simulations based on the finite-difference time-domain (FDTD) method, we performed a computational analysis of the dependence of the spectral properties of straight waveguides based on amorphous optical media on the waveguide width, the results of this investigation being summarized in Fig. S7. In particular, we present in this figure the transmission spectra of three such waveguides, with waveguide width, w, of $1.2\sqrt{3}a$ (831 nm), $1.3\sqrt{3}a$ (901 nm), and $1.4\sqrt{3}a$ (970 nm)[9]. For each waveguide, the transmission spectra were determined for several values of the propagation distance.

According to this analysis, for a propagation distance of $10.8\,\mu$m, the waveguide with $w = 831$ nm has a 3 dB bandwidth of 150 nm centered at 1483 nm, the waveguide with $w = 901$ nm has a 3 dB bandwidth of 203 nm centered at 1525 nm, and the waveguide with $w = 970$ nm has a 3 dB bandwidth of 130 nm centered at 1602 nm. As expected, a wider waveguide has a passband located at larger wavelengths, namely closer to the edge of the
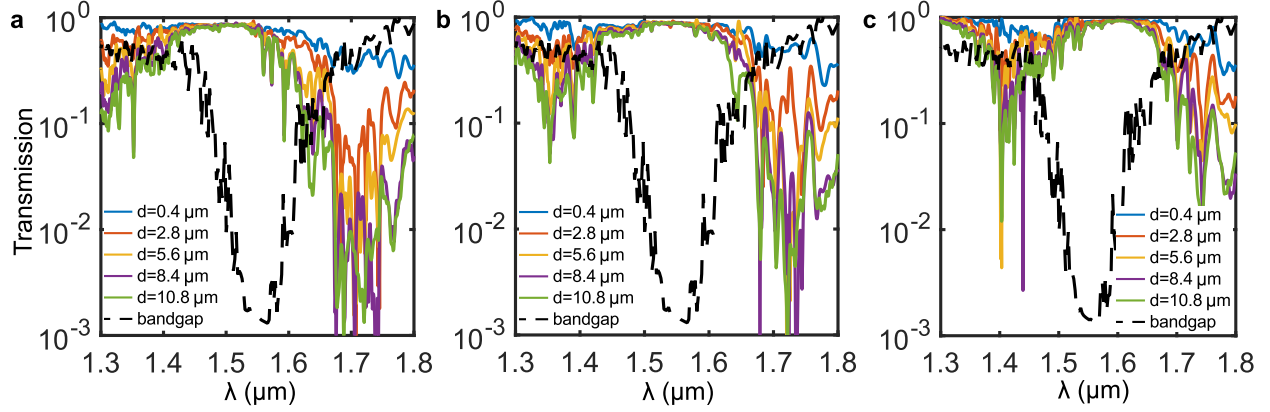
FIG. S7. (a), (b), (c) Transmission spectra of straight waveguides embedded in an amorphous structure, determined for $w = 831\,\text{nm}$, $w = 901\,\text{nm}$, and $w = 970\,\text{nm}$, respectively. The dashed lines indicate the transmission spectra through a section of amorphous crystal, whereas the distance from the excitation source is indicated in the legends.

dielectric band[5]. The extent of this passband is determined by the location of the band gap of the amorphous crystal, which is indicated in Fig. S7 by the dashed lines. Varying the waveguide width from $1.2\sqrt{3}a$ to $1.4\sqrt{3}a$ enables one to optimize the transmission properties of the waveguide, namely to minimize its optical losses, by aligning the waveguide passband with the band-gap of the embedding amorphous crystal.

SUPPLEMENTARY REFERENCES

[1]D. Frenkel and B. Smit, *Understanding molecular simulation: From algorithms to applications* (Academic Press, 2001).

[2]M. C. Sarihan, *Photonic integrated circuit components with amorphous structures*, Master's Thesis, Middle East Technical University, Ankara, Turkey (2018).

[3]S. G. Johnson and J. D. Joannopoulos, *Block-iterative frequency-domain methods for Maxwell's equations in a planewave basis*, Opt. Express **8**, 173 (2001).

[4]A. F. Oskooi, D. Roundy, M. Ibanescu, P. Bermel, J. D. Joannopoulos, and S. G. Johnson, *Meep: A flexible free-software package for electromagnetic simulations by the FDTD method*, Comput. Phys. Commun. **181**, 687 (2010).

[5]J. D. Joannopoulos, S. Johnson, J. N. Winn, and R. D. Meade, *Photonic crystals: molding the flow of light* (Princeton University Press; 2nd ed., March 2, 2008).

[6]T. Schwartz, G. Bartal, S. Fishman, and M. Segev, *Transport and Anderson localization in disordered two-dimensional photonic lattices*, Nature **446**, 52 (2007).

[7]I. Studenyak, M. Kranj, and M. Kurik, *Urbach rule in solid state physics*, Int. J. Opt. Appl. **4**, 76 (2014).

[8]H. Miyazaki, M. Hase, H. T. Miyazaki, Y. Kurokawa, and N. Shinya, *Photonic material for designing arbitrarily shaped waveguides in two dimensions*, Phys. Rev. B **67**, 235109 (2003).

[9]M. C. Sarihan, Y. B. C. Yilmaz, M. Erdil, M. S. Aras, C. Yanik, C. W. Wong, and S. Kocaman, *Flexible waveguides with amorphous photonic materials*, in Opt. Components Mater. XVI, edited by M. J. Digonnet and S. Jiang (SPIE, 2019), p. 35.